THE JOURNAL OF PHYSICAL CHEMISTRY B
A JOURNAL OF THE AMERICAN CHEMICAL SOCIETY

pubs.acs.org/JPCB

Article

Classical Molecular Dynamics Simulation of Glyonic Liquids: Structural Insights and Relation to Conductive Properties

Bai Hei, Jeanne E. Pemberton, and Steven D. Schwartz*

Cite This: *J. Phys. Chem. B* 2023, 127, 921−931

Read Online

ACCESS | Metrics & More | Article Recommendations | Supporting Information

ABSTRACT: Rhamnolipids are biosurfactants that have obtained wide industrial and environmental interests with their biodegradability and great surface activity. Besides their important roles as surfactants, they are found to function as a new type of glycolipid-based protic ionic liquids (ILs)—glyonic liquids (GLs). GLs are reported to have impressive physicochemical properties, especially superionic conductivity, and it was reported in experiments that specific ion selections and the fraction of water content have a strong effect on the conductivity. Also, the shape of the conductivity curve as a function of water fraction in GLs is interesting with a sharp increase first and a long plateau. We related the conductivities to the three-dimensional (3D) networks composed of −OH inside the GLs utilizing classical molecular dynamics (MD) simulations. The amount and size of these networks vary with both ion species and water fractions. Before reaching the first hydration layer, the −OH networks with higher projection/box length ratios indicate better conductivity; after reaching the first hydration layer and forming continuous structures, the conductivity retains with more water molecules participating in the continuous networks. Therefore, networks are found to be a qualitative predictor of actual conductivity. This is explained by the analysis of the atomic structures, including radial distribution function, fraction free volume, anion conformations, and hydrogen bond occupancies, of GLs and their water mixtures under different chemical conditions.

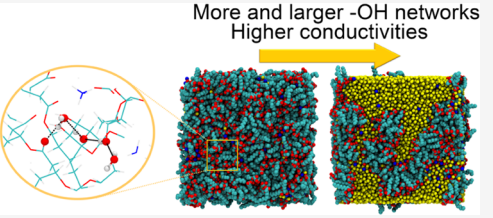

1. INTRODUCTION

Ionic liquids (ILs) are salts that remain in liquid state at or close to room temperature,[1] with melting points below 100 °C.[2] They exhibit unique physicochemical properties[3,4] including nonvolatility, nonflammability, air and water stability, tunability, and impressive electrical conductivity. As a result, ILs have seen use in a wide variety of applications,[2−5] such as the replacement of conventional volatile organic solvents, reaction media for chemical reactions, electrolytes, and gas absorption media. ILs are usually composed of two organic ions or a combination of one organic and one inorganic ions. Protic ILs (PILs), a subset of ILs, are produced by the simple acid−base reaction with a proton transfer process in the form of HA + B → HB^+ + A^-.[4] PILs tend to have lower melting points and higher conductivities.[6,7]

Rhamnolipids are a type of glycolipid that can be biologically produced by *Pseudomonas* species.[8] As a well-known biosurfactant, rhamnolipids are biodegradable and relatively nontoxic[9,10] and therefore have been studied and applied to a variety of industrial and environmental uses.[8,10−12] Also, numerous studies have been carried out to investigate the structures and morphologies of rhamnolipids,[13−22] especially computationally, at both vacuum−water[14,15,18] and oil−water[15] interfaces, and in rhamnolipid mixtures and solutions.[16−19] It was found that the conformations, interactions, and self-assembly structures can be greatly affected by salinity, ionization, and alkyl chain lengths.

Recently, a new kind of PILs termed glyonic liquids (GLs) has been created by combining rhamnolipid as the proton donor and an amine-containing moiety as the proton acceptor.[23] Superionic H^+ conductivity has been measured,[23] and the low cost and sustainability make these GLs a promising new material.

To study the structure of ILs, several models are proposed, including H-bonds and H-bond networks, ion pairs, and self-assembled nanostructures.[24] Radial distribution functions (RDFs) are often used to study interactions and aggregations.[25−28] Hydrogen bond occupancy is also affected by the ionicity and cation/anion selections[15] and is also studied.

Besides neat IL systems, a binary mixture of IL and water has also been widely studied with computer simulations.[29−40] It was found that water fractions,[31−35,38−40] ion species,[29,38] alkyl chain lengths,[38] and hydrophobicities[33] can affect the hydrogen bonding, nanostructuring, ion diffusions, densities, viscosities, and other interactions, structures, and dynamics of the ILs.

Three-dimensional (3D) network structures are found in a variety of similar conductive systems,[27,41−43] especially with the participation of water. Also, water and hydrogen bond channels/clusters/networks are usually recognized as the key

Received: October 15, 2022
Revised: January 4, 2023
Published: January 18, 2023

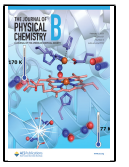

Table 1. Composition, Dimension, and Estimated Density of Each Simulated System at Room Temperature

system	molecules number	initial box size (Å^3)	final box size (Å^3)	estimated density (g/mL)
$(NH_4)^+$(Rha-C10)$^-$	1200, 1200	100 × 100 × 100	88.42 × 88.25 × 88.25	1.02
$(t$BuNH$_3)^+$(Rha-C10)$^-$	1000, 1000	100 × 100 × 100	88.90 × 88.89 × 88.94	0.963
$(t$BuNH$_3)^+$(Rha-C10)$^-$ + Rha-C10 9:9:1	900, 900, 100	100 × 100 × 100	90.19 × 90.24 × 90.19	0.996
$(t$BuNH$_3)^+$(Rha-C10)$^-$ + Rha-C10 1:1:1	600, 600, 600	100 × 100 × 100	89.86 × 89.86 × 89.82	1.02
$(NH_4)^+$(Rha-C10C10)$^-$	800, 800	100 × 100 × 100	88.80 × 88.74 × 88.74	0.991
$(NH_4)^+$(Rha-C10C10)$^-$ + 0.5 mol H_2O/mol GL	800, 800, 400	100 × 100 × 100	88.39 × 88.30 × 88.30	1.02
$(NH_4)^+$(Rha-C10C10)$^-$ + 20 mol H_2O/mol GL	600, 600, 12,000	100 × 100 × 100	93.80 × 93.82 × 93.82	1.06
$(NH_4)^+$(Rha-C10C10)$^-$ + 100 mol H_2O/mol GL	200, 200, 20,000	100 × 100 × 100	90.85 × 90.93 × 90.93	1.03
$(t$BuNH$_3)^+$(Rha-C10C10)$^-$	800, 800	100 × 100 × 100	91.44 × 91.49 × 91.50	1.00
$(t$BuNH$_3)^+$(Rha-C10C10)$^-$ + 0.5 mol H_2O/mol GL	800, 800, 400	100 × 100 × 100	92.53 × 92.55 × 92.46	0.984
$(t$BuNH$_3)^+$(Rha-C10C10)$^-$ + 20 mol H_2O/mol GL	600, 600, 12,000	100 × 100 × 100	96.34 × 96.31 × 96.37	1.04
$(t$BuNH$_3)^+$(Rha-C10C10)$^-$ + 100 mol H_2O/mol GL	200, 200, 20,000	100 × 100 × 100	91.84 × 91.84 × 91.91	1.02

to superionic conductivities,[25,26,42,44,45] corresponding to the Grotthuss mechanism. However, those methods usually focus on the bulk structure or the water channels only. The structural frame formed by the connections between polar atoms, the vacancies, the hydrogen bonds, and the hydroxyl groups interacting with water inside GLs are all related to the performance of the material. We thus study these qualitative features found in GLs to direct on proton transport and conductive properties.

To be more specific, four major questions are addressed here—(i) how to simply relate the molecular dynamics (MD) simulation trajectories to the actual conductivities; (ii) how to explain the dramatic increase of conductivity when only a small portion of water is added to GLs; (iii) how to explain the retained conductivity when a high fraction of water is added; and (iv) how the dynamics of anion conformations and hydrogen bonds affect the conductivity. Properties are found that address these questions, and also, we make some predictions regarding the ion species based on their effects on relative properties.

2. METHODS

2.1. Classical Molecular Dynamics (MD) Simulations. We carried out a classical molecular dynamics study on a series of GL systems listed in Table 1. These systems are composed of different kinds of cations and anions. Water has a great influence on the properties, so it is also included. The structure of each component is displayed in Chart 1. For each simulation, the initial system was prepared using PACKMOL software,[46] with the indicated number of cations, anions, and neutral molecules randomly distributed in a 100 × 100 × 100 Å^3 cubical box with a 2 Å tolerance that defines the minimum distance between any two atoms. Then, the standard procedure for the MD simulation was conducted in nanoscale molecular dynamics (NAMD)[47] with periodic boundary conditions in all three dimensions. The system was first minimized for 30,000 steps (1 fs/step), then heated to room temperature (300 K) with a rate of 0.5 K/ps, and then equilibrated for 100−125 ns. The other simulation parameters are the same as our former work[15] on monorhamnolipids. The force field for NH_4^+ is given in Chemistry at HARvard Macromolecule Mechanics (CHARMM)[48] additive force field files.[49] The other force field parameters are obtained from the CHARMM general force field (CGenFF).[48−50] The force field parameters of tBuNH$_3^+$ were further optimized using the force field toolkit[51] to amend the poor analogy with high charge penalty and reproduce the property at a high level of ab initio calculation.[15,52] After the total energy came to a plateau, the system was fully equilibrated, and another 50 ns simulation was conducted as the "production" part to generate trajectories for further analysis. The trajectories are saved in 500 frames with a 0.1 ns gap. After equilibration, the size of the cubical box containing GLs shrank, leading to estimated densities of ∼1 g/cm^3, which agrees well with the density measured in experiments. This validated the force field parameters and indicated that the ions in the box were tightly packed.

Chart 1. Structures of Anions, Cations, and Neutral Molecules, Oxygen Assignments (Red), and Carbon Assignments (Black)

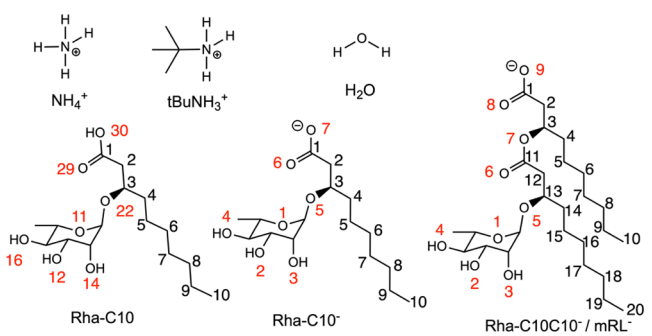

2.2. Water Fraction. The experimental results indicated that the fraction of water plays a significant role in the conductivity of GL. Therefore, we investigated the atomic structures of a series of GLs with different fractions of water. We chose four systems—neat GLs, a small fraction of contamination (0.5 mol H_2O/mol GL), a fraction of water associated with the first hydration layer (20 mol H_2O/mol GL), and a large fraction of water (100 mol H_2O/mol GL) that preserve similar or even higher conductivity. The details of the first hydration layer water fraction determination are shown in Figures S1 and S2.

2.3. 3D Network. It was reported that 3D chains/network structures were found in water and Nafion[41,42] or ionic liquid mixtures.[27,53−55] These structures are also related to proton transport. Here, we set the connectivity criterion as a distance of 3 Å or less based on radial distribution functions we obtained and hydrogen bond lengths. There are also some exceptions—interactions between two oxygens with no hydrogen, and two oxygens located on the same sugar ring that are originally within 3 Å of each other are excluded. After obtaining the connections of all investigated atoms, we used a depth first search (DFS) method to obtain the network size

https://doi.org/10.1021/acs.jpcb.2c07264
J. Phys. Chem. B 2023, 127, 921−931

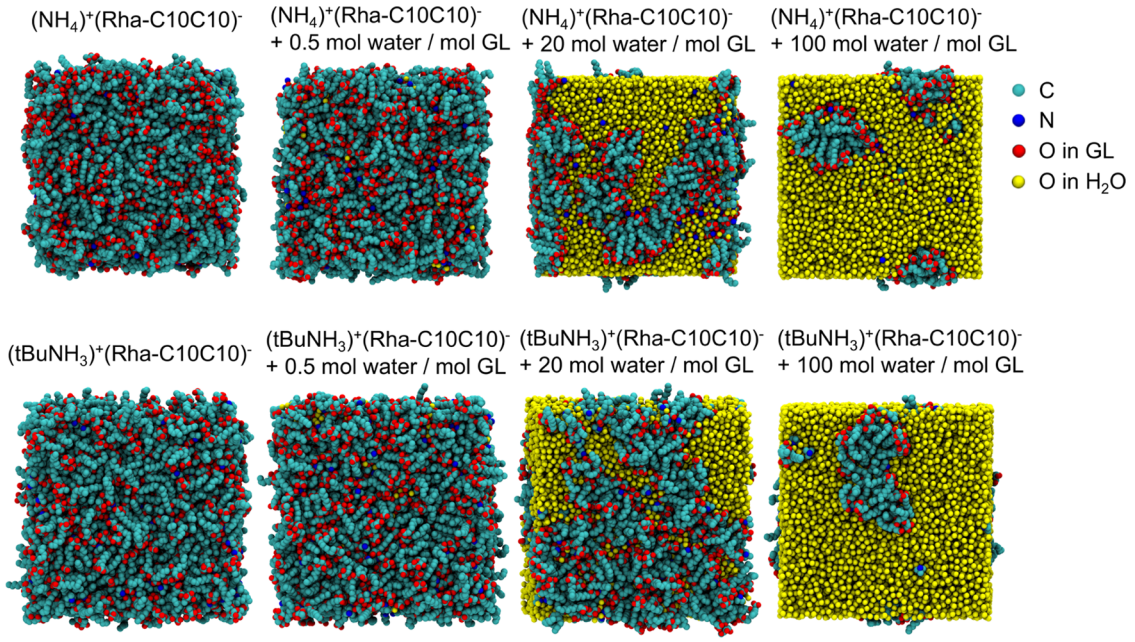

Figure 1. Representative snapshots of equilibrated simulation boxes of $(NH_4)^+$(Rha-C10C10)$^-$ and $(t\text{BuNH}_3)^+$(Rha-C10C10)$^-$ with water fractions of 0, 0.5 mol/mol of GL, 20 mol/mol of GL, and 100 mol/mol of GL. Water molecules are shown in yellow spheres. Hydrogen atoms are removed for clarity.

distribution of each system. With the DFS method, a random atom was selected as a root node, then it was marked as visited. Each branch of this root node was explored by visiting each unvisited node connected to the root. New nodes were added to the stack and marked as visited. If a node has no unvisited node connected to it, this branch is done, and we backtracked to the last visited node. By repeating these steps, the whole network including that node was explored with the longest branch first. All polar atoms are investigated to make sure that all of the networks are explored. The projection of each network on the *x*-, *y*-, or *z*-axes, which is the largest distance between the orthographic projections of all of the oxygen coordinates on one dimension of that network, is calculated by subtracting the maximum coordinate by the minimum coordinate on the corresponding axis. We saved the total number of atoms, as well as the projections on each axis of each network for further analysis. The fraction of the simulation box that can be covered by a network, or the coverage fraction F_n, where $n = x$, y, or z, is calculated by the network projection/the length of the simulation box on the *x*-, *y*-, or *z*-axis.

2.4. Fraction Free Volume (FFV) Calculation. Free volume relates to important properties such as gas solubility,[28,56] damping property,[57] and conductivity.[58] To obtain FFV from simulation results, we created a mesh of grid points over a 40 × 40 × 40 Å^3 box centered in the simulation box of each frame. A total volume of 3.2 × 10^7 Å^3 was analyzed for each system. Each grid point is 1 Å away from the nearest six points. If one grid point is not within the van der Waals radii of any atoms, it is defined as a part of the free volume.[59] The fraction of mesh points belonging to free volume is FFV. The van der Waals radii we used for H, O, C, and N are 1.20, 1.52, 1.70, and 1.55 Å, respectively.[60]

2.5. Cavity and Vacancy Size Distribution. Here, we introduce two new metrics, cavity size[28] and vacancy size.[61] The method we used to measure FFV can be regarded as using a probe with a radius of 0 Å. The cavity size radius is obtained by calculating the maximum probe size at each grid point[28] without touching the van der Waals surface of any nearby atom. The cavity size can be regarded as the largest probe that can be put at each grid point.

Since atoms are regarded as spheres, the free volume inside GLs is percolated,[61] as shown in Figure S3, so the vacancies with different sizes are connected to each other. Based on the calculations in Figures S3 and S4, the percolation starts to reduce at a probe radius of about 0.35 Å and a rough estimation for a proper probe is 0.6 Å. So, we used a probe with a 0.6 Å radius to reduce the effects of percolations and obtained the distributions of the major vacancies.[61] The vacancy size can be regarded as the volume of each major vacancy.

With these two metrics, the shape of the vacancies can be induced. Large cavity size indicates large sphere-shaped free space in the structure, while small cavity size with large vacancy size suggests narrow but continuous free volume.

3. RESULTS AND DISCUSSION

Experimentally, the conductivity is closely related to water fraction, with a sharp increase at the beginning and surprisingly relatively constant conductivity even when the water fraction is high.[23] So, we studied the effects of impurity water and captured the network structure formed inside GLs with different water fractions. Water also has effects on molecular conformations and dynamics. For the neat GL system, we studied the effects of different cation and anion species on free volumes. These all give us clues to determine the conductivities.

3.1. 3D Networks and Conductivities. We first conducted MD simulations on $(NH_4)^+$(Rha-C10C10)$^-$ and $(t\text{BuNH}_3)^+$(Rha-C10C10)$^-$ with water fractions of 0, 0.5 mol/mol, 20 mol/mol, and 100 mol/mol of GL. In experiments, as the water fraction increases, conductivity will sharply increase first and then reach a plateau at around 20 mol of water/GL.[23]

https://doi.org/10.1021/acs.jpcb.2c07264
J. Phys. Chem. B 2023, 127, 921−931

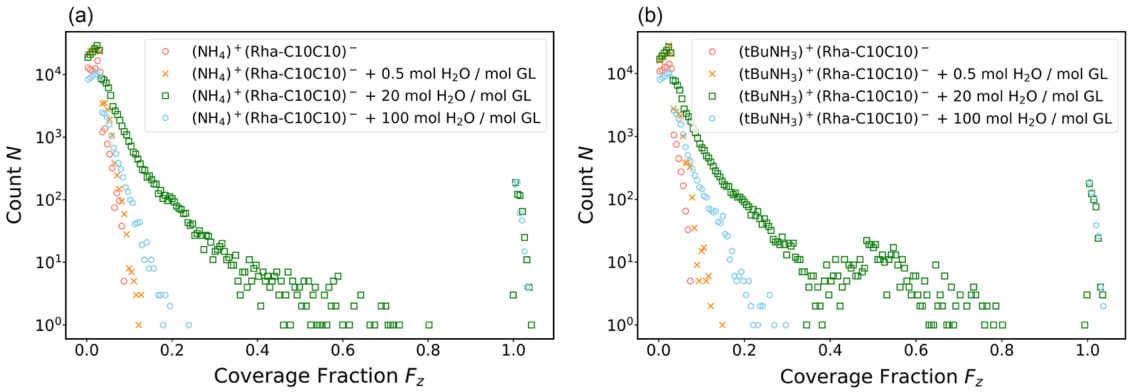

Figure 2. Distributions of the coverage fraction F_z on the z-axis, calculated by the projection length/box length on the z-axis, of the networks composed of −OH, in $(NH_4)^+(Rha\text{-}C10C10)^-$ (a) and $(tBuNH_3)^+(Rha\text{-}C10C10)^-$ (b) with water fractions of 0, 0.5 mol/mol of GL, 20 mol/mol of GL, and 100 mol/mol of GL. The Y-axis is the total count N of networks at the presenting coverage fractions over 500 frames. When the water fraction reaches the first hydration layer, networks expand to the whole simulation box and lead to F_z around 1.0. After that, with more water added, there are fewer networks with F_z smaller than 1.0 because more and more atoms are participating in the networks that cover the entire box.

The turning point is around the first hydration layer, which indicates the importance of the consecutive networks formed mainly by water. We found that the networks composed of −OH groups (including water), which can provide proton transport pathways, are highly correlated with conductivities.

With the water fraction increasing, water molecules and the hydrophilic part of GL form more connections. Figure 1 presents representative snapshots of the simulation boxes. The snapshots of neat GLs $(NH_4)^+(Rha\text{-}C10)^-$ and $(tBuNH_3)^+(Rha\text{-}C10)^-$ are shown in Figure S5. Polar atoms aggregate together, and channels of different shapes start to form in the boxes at the edge of the hydrophilic part of GLs. In a single simulation box, the total number of polar atoms in one network can reach 1.52×10^4 for 20 mol water/mol of $(NH_4)^+(Rha\text{-}C10C10)^-$ and 2.08×10^4 for 100 mol water/mol of $(NH_4)^+(Rha\text{-}C10C10)^-$. These networks connect through the whole simulation box.

The Grotthuss mechanism is regarded as a significant part of proton transport employing −OH channels/bridges.[62,63] So, we choose projections of −OH networks as a qualitative method to examine conductivities. Here, water has −OH in it and is also included. As shown in Figure S6, continuous architectures can be formed like the other ILs or conductive binary mixtures[27,41,64] within the scale of the simulation box. The distributions of these network projections on the z-axis are shown in Figure 2. The distributions on other axes are in Figure S7.

For both $(NH_4)^+(Rha\text{-}C10C10)^-$ (Figure 2a) and $(tBuNH_3)^+(Rha\text{-}C10C10)^-$ (Figure 2b), when the water fraction increases from 0 to 0.5 mol water/mol of GL, both the amount and coverage fractions (projection length/box length) of −OH networks increase. As the water fraction gets larger to 20 and 100 mol water/mol of GL, the size in space of the networks reached the simulation box size, resulting in the coverage fractions around 1, making the −OH clusters connecting through the whole material, and more and more atoms are included in these networks as the count of networks with coverage fractions smaller than 1 decreases. The box length is obtained from the periodic boundary cell size, but if a molecule is crossing the boundary of the simulation box, it will not be cut apart and the Cartesian coordinates we obtain will exceed the box range, resulting in the points with coverage fractions larger than 1, but they are effectively 1. The average aggregation size, S_{mean}[25] (continuous networks crossing the whole simulation box are excluded), of −OH networks (Table 2), also reflects the same trend. S_{mean} is calculated by $S_{mean} = \sum n_s S^2 / \sum n_s S$,[25] where S is the number of −OH in one network, and n_s is the count of networks with that number of −OH over 500 frames (50 ns). The average aggregation size increases first and then decreases because more atoms are participating in the continuous networks and the calculation is based on noncontinuous networks only. This agrees well with experimental results in the patent—the conductivity increases as water fraction increases, reaches a plateau, and holds that conductivity at around 20 mol water/mol of GL, as indicated by the networks with coverage fractions of 1.

Table 2. Average Aggregation Size S_{mean} of −OH Clusters[a]

water fraction	$(NH_4)^+$ $(Rha\text{-}C10C10)^-$	$(tBuNH_3)^+$ $(Rha\text{-}C10C10)^-$
0	2.42	2.35
0.5 mol H_2O/mol GL	2.60	2.61
20 mol H_2O/mol GL	31.9	112
100 mol H_2O/mol GL	4.47	7.05

[a]Continuous networks with more than 1000 atoms are excluded.

$(NH_4)^+(Rha\text{-}C10C10)^-$ and $(tBuNH_3)^+(Rha\text{-}C10C10)^-$ have similar distributions of −OH networks for the same water fraction, and $(tBuNH_3)^+(Rha\text{-}C10C10)^-$ is slightly more enriched in both amount and size. $(tBuNH_3)^+(Rha\text{-}C10C10)^-$ has larger clusters when water is added because of the optimal structures that will be discussed later. We therefore make the assumptions that with the same water fractions, $(NH_4)^+(Rha\text{-}C10C10)^-$ and $(tBuNH_3)^+(Rha\text{-}C10C10)^-$ have similar conductivities and the conductivities of $(tBuNH_3)^+(Rha\text{-}C10C10)^-$ are slightly higher than those of $(NH_4)^+(Rha\text{-}C10C10)^-$.

Vehicle transport can also contribute to total conductivity. So, we also compared the root-mean-square deviations (RMSDs) of cations and water between two GLs with different water fractions (Figure 3). When the water fraction is low, NH_4^+ is more confined within the structure (Figure 3a), which stabilizes the network structures and explains the sharp increase at the beginning of water addition. As the water fraction gets higher, NH_4^+ is more likely to be dissolved by water, as shown in Figure 1, and therefore has a larger RMSD.

https://doi.org/10.1021/acs.jpcb.2c07264
J. Phys. Chem. B 2023, 127, 921−931

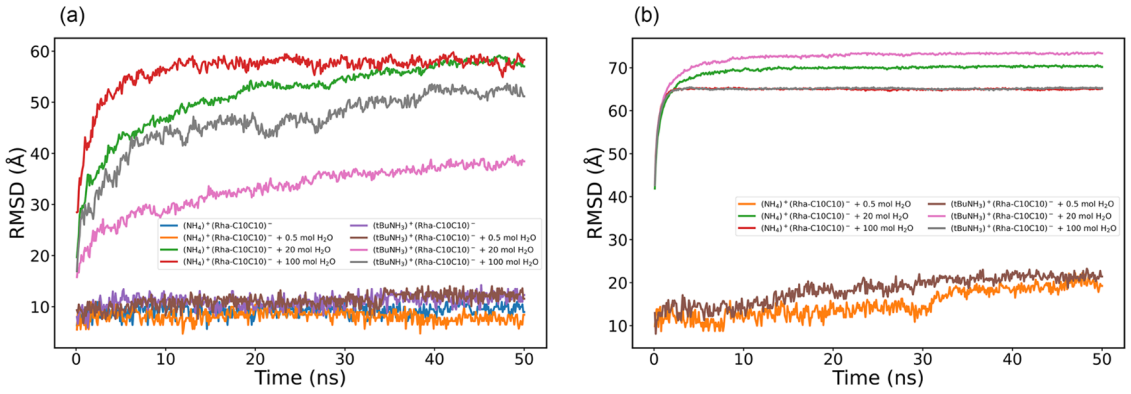

Figure 3. RMSD of cations (a) and water (b) in $(NH_4)^+(Rha\text{-}C10C10)^-$ and $(tBuNH_3)^+(Rha\text{-}C10C10)^-$ with water fractions of 0, 0.5 mol/mol of GL, 20 mol/mol of GL, and 100 mol/mol of GL.

Meanwhile, the restriction from the hydrophobic part of $tBuNH_3^+$ apparently limited its solubility and migrations. But still, for both of them, as water fraction continuously increases, ions are dissolved and diluted. However, the conductivity does not decrease, so the Grotthuss mechanism led by −OH networks becomes dominant and makes major contributions to the conductivities.

At a fraction of 0.5 mol water/mol of GL, water in $(tBuNH_3)^+(Rha\text{-}C10C10)^-$ systems has a higher RMSD than in $(NH_4)^+(Rha\text{-}C10C10)^-$. One possible reason is that the HBs are more dedicated and the vacancies are larger in neat $(tBuNH_3)^+(Rha\text{-}C10C10)^-$, providing more space for water to migrate. As the water fraction increases to 20 and 100 mol water/mol of GL, the migrations of water become similar. This indicates the similarity of a subportion of the −OH network—water clusters—among the large water fraction range and supports that −OH networks are a great indicator of conductivities.

Thus, the coverage fraction of −OH networks, which can be conveniently obtained from MD trajectories and is suitable for visualization, is proved to be a good indicator of conductivities.

3.2. Effects of Different Cation and Anion Species on Free Volume in Neat GLs. Besides conductivity, free volume is another major difference between the GL systems we investigated and explains the conductivities with small water fractions.

3.2.1. FFV and Vacancy Distribution. We investigated the free volume and its distribution inside each system. GL systems have a relatively large FFV (Figure 4), which suggests a good gas absorption capacity.[28] GLs with NH_4^+ as cations tend to have smaller FFV than those with $tBuNH_3^+$ because NH_4^+ has a smaller size and can fit into void spaces. The conformation information and lower HB occupancies also show a higher interactivity of NH_4^+, which makes it easier for NH_4^+ to fit in.

By calculating the maximum probe size at each grid point[28] without touching the van der Waals surface of any nearby atom and by calculating the volume of vacancies using a larger probe size of 0.6 Å to reduce percolations,[61] we obtained the distributions of the cavity size radius (Figure 5a) and the vacancy size distributions (Figure 5b), as mentioned in Section 2. At a cavity size of 2.0−2.5, $(tBuNH_3)^+(Rha\text{-}C10)^-$ has about 10 times more cavities than the other GLs. While at a vacancy size of 200−700, GLs with $(tBuNH_3)^+$ as cations have about 2−5 times vacancies at a certain size as the other GLs. From these distributions, we can see that the larger FFV of $(tBuNH_3)^+(Rha\text{-}C10)^-$ comes from both the larger distances

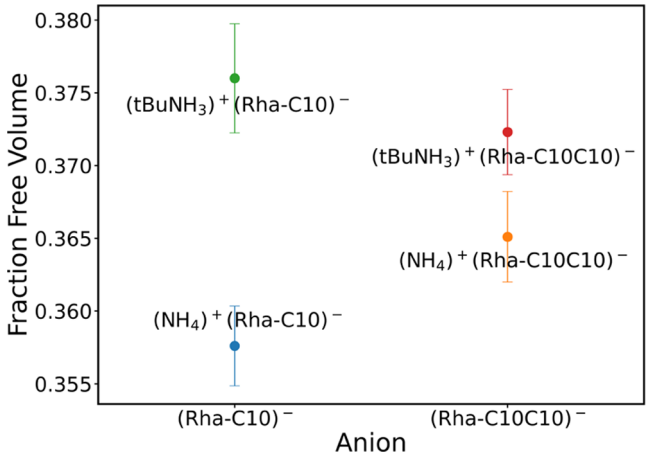

Figure 4. Fraction free volumes of four kinds of neat GLs.

between atoms and the larger volume of void holes inside it, while the larger FFV of $(tBuNH_3)^+(Rha\text{-}C10C10)^-$ is only because of the continuous vacancies formed in the network structure.

The effects of $Rha\text{-}C10^-$ and $Rha\text{-}C10C10^-$ are related to the hydrophilic/hydrophobic properties of the cations. We have the hypothesis that $Rha\text{-}C10C10^-$ is more flexible in space and can surround $tBuNH_3^+$ (Figure S8); thus, the cavity size radius decreases because of tighter packing. This is not observed in GLs with NH_4^+. The more steady alkyl chains and higher HB occupancies (will be discussed later) reveal that $(tBuNH_3)^+(Rha\text{-}C10C10)^-$ forms more solid network structures inside, so the vacancy size remains large. NH_4^+ is more likely to gather oxygens and avoid being surrounded by alkyl chains. When the anion changes from $Rha\text{-}C10^-$ to $Rha\text{-}C10C10^-$, the extra alkyl chain hollows out the structure and leads to a higher FFV.

GLs with a larger free volume and more polar atoms left along because of the repulsion can provide more space and interactive positions for water and contribute to higher conductivity when water is added. This matches the trend we found in −OH networks—with a continuous narrow-shaped larger free volume, $(tBuNH_3)^+(Rha\text{-}C10C10)^-$ has a larger coverage fraction that contributes to conductivity. So, we believe that the FFV of neat GL explains the sharp increase of conductivity at the beginning of water addition.

3.3. Atomic Level Structure and Conformation of the Neat GLs. In this section, we studied the RDFs, anion

https://doi.org/10.1021/acs.jpcb.2c07264
J. Phys. Chem. B 2023, 127, 921−931

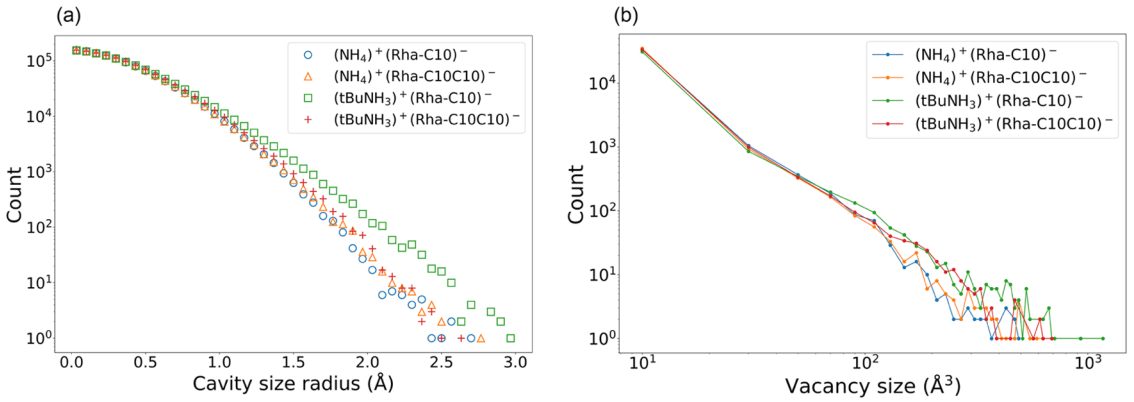

Figure 5. Cavity size radius (a) and vacancy distributions (b) of four kinds of neat GLs. Here, the cavity size can be regarded as the largest sphere that can be put on a grid point, while the vacancy size is the volume of each major vacancy. The *Y*-axis is the total count of cavities or vacancies over 500 frames.

conformations, and HB occupancies, which indicate that different anions and cations lead to different spatial occupation patterns and explain the differences in FFV.

3.3.1. N−N and N−O RDF. We first compared the radial distribution function (RDF) of N−N in $(NH_4)^+$(Rha-C10)$^-$, $(tBuNH_3)^+$(Rha-C10)$^-$, $(NH_4)^+$(Rha-C10C10)$^-$, and $(tBuNH_3)^+$(Rha-C10C10)$^-$. The distribution of nitrogen reflects the distribution of cations. As shown in Figure 6, the

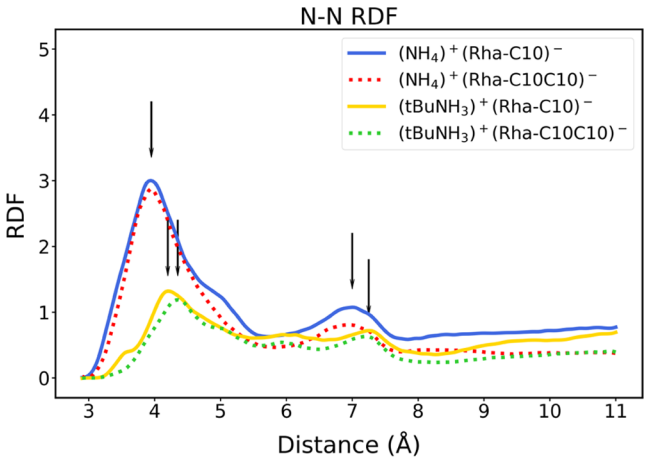

Figure 6. N−N RDF of four different GLs. The bulky cation will lead to a slightly higher peak position and lower peak. The bulky anion will also lead to a decrease in RDF.

bulky cation leads to a slightly higher peak position and lower peak, which indicates that they are further away from each other, and $tBuNH_3^+$ is more difficult to be gathered around the same anion because of the bulkiness. The bulky anion also leads to a decrease in RDF, which means they also contribute to blocking the cations. The N−O RDF (Figure S9) reflects the interactions between cations and anions. By comparing the height of peaks in RDFs of N interacting with all oxygens, we found that the interaction between cations and carboxyl oxygens is dominant, with a high and sharp peak at about 2.7 Å. With bulkier ion species, the importance of this interaction is more obvious—a bulkier structure limited the interactions between cations and hydroxyl or ether oxygens more, both in distance and in population, leading to larger FFV.

3.3.2. Anion Conformation. The distributions of the lengths of the alkyl chains do not show large variation among different anions or cations (Figure S10), so the folding degree of the alkyl chain does not change with cation or anion selections.

The C−C distance distribution of the two carbons, C10 and C20, on two terms of alkyl chains (Figure 7a) reflects the conformation of the hydrophobic part of the rhamnolipids. With a bulkier cation, the two alkyl chains tend to be either parallelly aligned together or stretched into two different directions with other alkyl chains inserted in between. That is because NH_4^+ can interfere with the interaction between oxygens and nitrogens, so the tweezer-like rhamnolipids can be either close or open and can move more flexibly and lead to a more flattened distribution. The C10−C20 peak at 15 Å indicates that with less rigidness, Rha-C10C10$^-$ can wrap around $tBuNH_3^+$, leading to tighter packing and less free volume than $(tBuNH_3)^+$(Rha-C10)$^-$. The two further apart peaks also reveal the steadier conformation of Rha-C10C10$^-$, which is good for network formation.

The intramolecular O−O distance distribution of the nearest distance between terminal carboxyl oxygens (O6 and O7 in Rha-C10$^-$ and O8 and O9 in Rha-C10C10$^-$) and rhamnose hydroxyl oxygens (O2, O3, and O4) in each anion (Figure 7b) is obtained by calculating all six O−O distances and select the smallest one (the six calculated distances are shown in Figure S11). This reflects the conformation of the hydrophilic area of each anion. The three peaks from left to right correspond to the direct interaction between carboxyl oxygens and hydroxyl oxygens, the carboxyl and hydroxyl oxygens connected by one NH_4^+ or $tBuNH_3^+$, and a completely open conformation. For Rha-C10$^-$, the peak at 2.65 Å is much smaller because of its rigidness. For Rha-C10C10$^-$, the peaks at 4.12 and 7.22 Å switched with NH_4^+ and $tBuNH_3^+$. When an NH_4^+ is interacting with the carboxyl oxygen, it is very likely to also attract the hydroxyl group (with either O2, O3, or O4 as oxygen) on the other side. However, $tBuNH_3^+$ is more likely to repel the hydroxyl oxygen with its bulky hydrophobic tail. The hydrophilic part of anions is affected by cations and with $tBuNH_3^+$, the further aparted hydrophilic part not only contributes to larger FFV but also leaves more sites to interact with water.

3.3.3. HB Occupancies. HBs here are defined with a criterion of 3 Å or less HB length and a H−O−O angle of 20° or less.[15] Occupancy is the percentage of time that the HB between two atoms or molecules retains. The higher the occupancy, the longer the HB retains. The HB occupancy

https://doi.org/10.1021/acs.jpcb.2c07264
J. Phys. Chem. B 2023, 127, 921−931

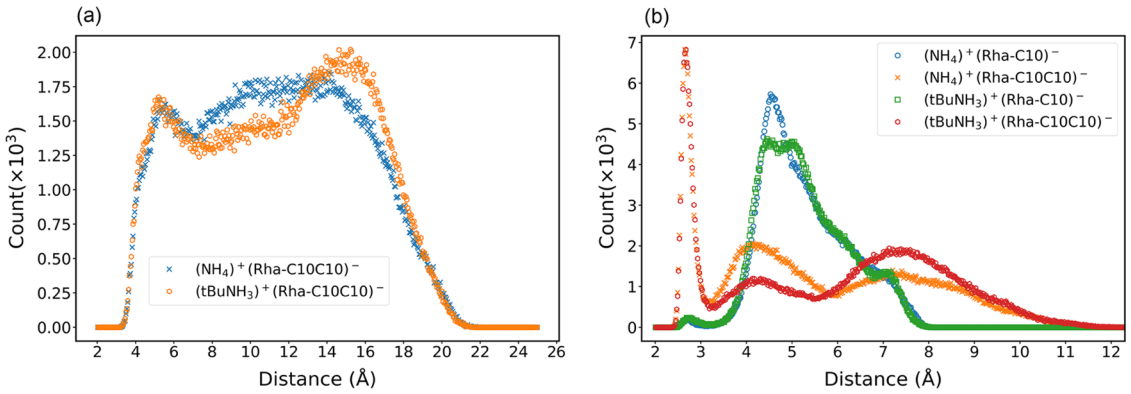

Figure 7. (a) C10−C20 distribution of two GLs with different cations. (b) O−O distribution between carboxyl oxygens (O6 and O7 in Rha-C10$^-$ and O8 and O9 in Rha-C10C10$^-$) and hydroxyl oxygens (O2, O3, and O4) of four GLs. The *Y*-axis is the total count of molecules normalized to 1000 molecules per simulation box over 500 frames.

higher than 100% means that the donor (or acceptor) is interacting with more than one acceptor (or donor) in one molecule. With these definitions, we evaluated the occupancies of all possible HBs formed between cations and anions in different systems. In Figure 8, the HBs in GLs with *t*BuNH$_3^+$ as

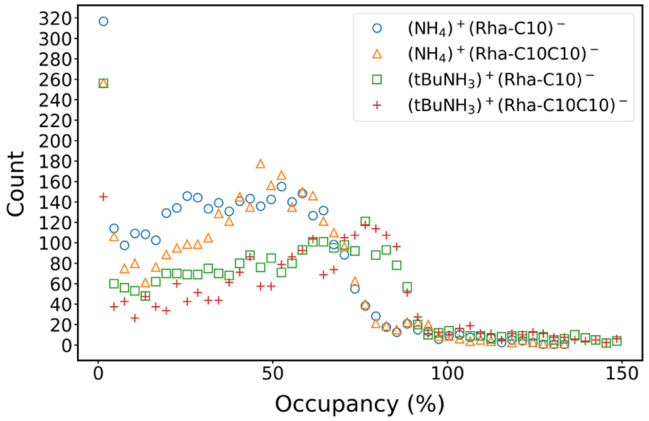

Figure 8. Occupancies of hydrogen bonds between cations and anions in $(NH_4)^+$(Rha-C10)$^-$, $(t\text{BuNH}_3)^+$(Rha-C10)$^-$, $(NH_4)^+$(Rha-C10C10)$^-$, and $(t\text{BuNH}_3)^+$(Rha-C10C10)$^-$. The *Y*-axis is the total count of hydrogen bonds normalized to 1000 GL molecules per simulation box over 500 frames.

cations tend to peak at higher occupancies (at 80%) than GLs with cation NH_4^+ (at 50%), with about 2−5 times the amount of HBs as GLs with NH_4^+ at an 80% occupancy, and are therefore more dedicated. The bulkiness of *t*BuNH$_3^+$ limits its choices and reduces its movements, so it is more focused on interacting with the same carboxyl oxygens than NH_4^+ (Figure S12) and thus reinforces the structures. As shown before, NH_4^+ has lower mobility when water is not present. It shifts hydrogen bond (HB) acceptors more frequently but is also easier to be captured by another acceptor and is actually more confined in the structure. Compared to Rha-C10$^-$, Rha-C10C10$^-$ does not have much effect on HBs with high occupancies but it can greatly reduce short-term HBs with occupancies lower than 40% by one-third. An additional alkyl chain limits the freedom of ions to form a different pair, thus helping it to stabilize the overall HBs within one GL pair and helping with the structure that maintains high FFV.

To sum up, in the neat GLs, RDFs, anion conformations, and HB occupancies are crucial for FFV and the formation of −OH networks with a small fraction of water.

3.4. Conformation and Dynamics of Rha-C10C10$^-$ with Different Water Fractions. The changes in conductivity and the network size reflected by the projection coverage ratio when water is added to the GLs can also be interpreted by the atomic level structure and conformation of the systems themselves.

3.4.1. Anion Conformation. Figure 9 shows the distance distribution between carboxyl (O8, O9) and hydroxyl oxygens (O2, O3, O4) (Figure 9a), between two alkyl chain tails (C10 and C20) (Figure 9b), and between the head and tail of each alkyl chain (C3 and C10, C13 and C20, respectively) (Figure 9c). From Figure 9a, we can see that the direct interaction between carboxyl oxygen and hydroxyl oxygen within one molecule first decreases with a higher water fraction. After reaching the first hydration layer, the peak increases as alkyl chains becomes more parallel (Figure 9b). The change in the second and the third peaks is because water provides more bridges to connect two oxygens. A close conformation of the hydrophilic part opens and participates in the −OH networks. Figure 9b indicates that the conformation of the hydrophobic part is a balance between the aggregation and disruption induced by water. A small addition of water (0.5 mol) and a large amount of extra water (100 mol) can both make the alkyl chains more parallel. As for Figure 9c, it shows that the alkyl chains are more flexible at a lower water fraction (0 and 0.5 mol) with wider peaks because of the more confined parallel aggregation conformation with more water and again stabilizes the network structure. Like the RMSD of water, the similarity of 20 and 100 mol water fractions in Figure 9a,c again explains the retained conductivities from another aspect.

3.4.2. Dynamics. The standard deviations of the nearest distance between carboxyl (O8, O9) and hydroxyl oxygens (O2, O3, O4) (Figure 10a), the distance between two alkyl chain tails (C10 and C20) (Figure 10b), and the length of alkyl chains (C3 and C10, C13 and C20, respectively) (Figure 10c) over 50 ns (same as the distances in Figure 9) are calculated; 20 mol and 100 mol H_2O/mol of GL can largely increase the variability of the anions because the environment is less rigid and the water is acting as a lubricant, but a small additive of 0.5 mol H_2O/mol of GL is more likely to aggregate the hydrophilic compartments together and restrict the movements.

https://doi.org/10.1021/acs.jpcb.2c07264
J. Phys. Chem. B 2023, 127, 921−931

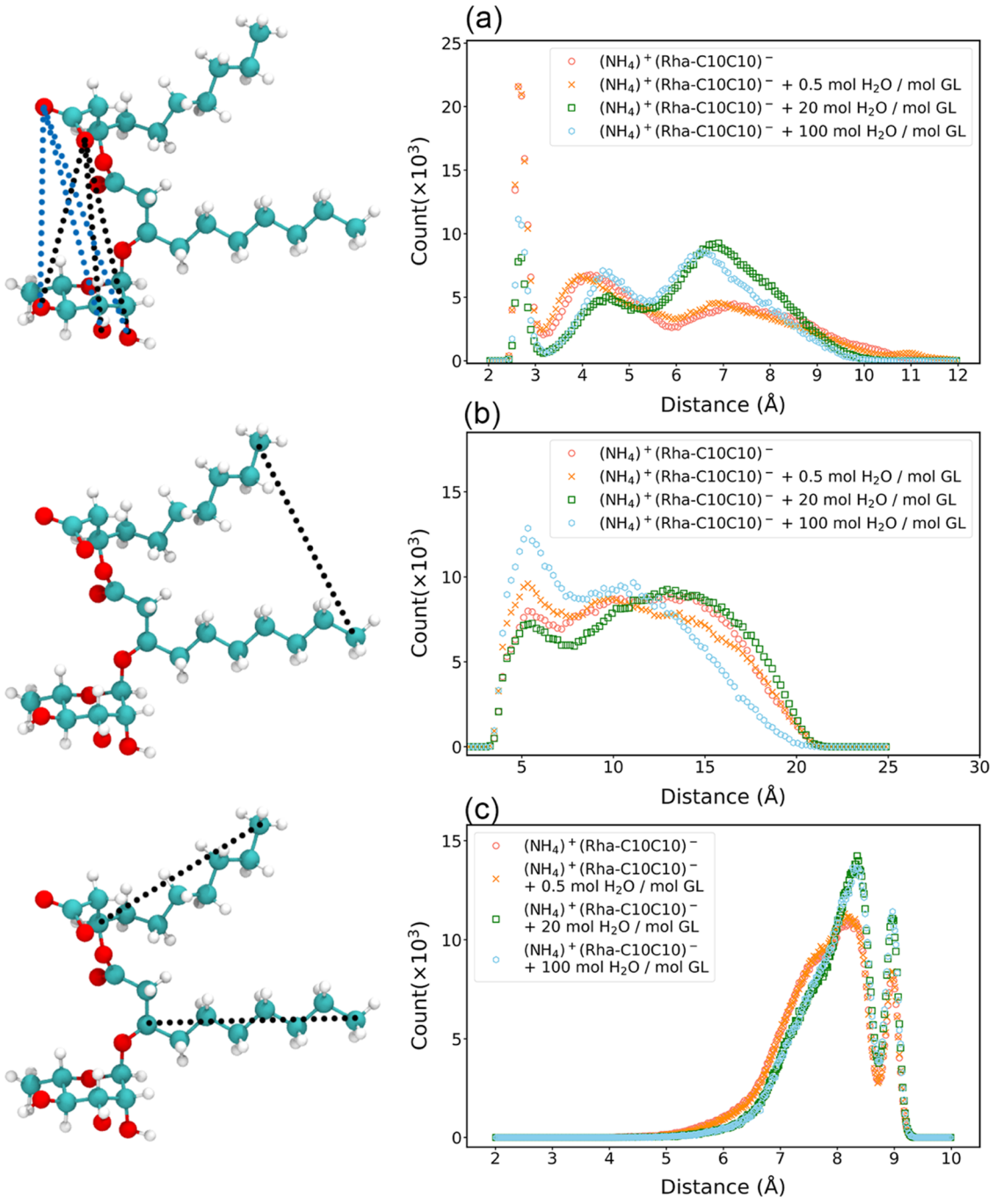

Figure 9. Distance distributions between the carboxyl and hydroxyl oxygens (a), between alkyl chain tails (b), and between the head and tail of each alkyl chain (c) of $(NH_4)^+(Rha\text{-}C10C10)^-$ with four water fractions. The *Y*-axis is the total count of molecules normalized to 1000 GL pairs per simulation box over 500 frames.

3.4.3. HB Occupancies. The change in dynamics is related to HB occupancies (Figure S15). The fraction of 0.5 mol H_2O/mol of GL retains long occupancies and introduces more HBs into the system, especially for HBs with occupancies smaller than 40%. Similar effects are also found with extra neutral species (Figure S9). This helps in a steadier network structure. The projections on the *z*-axis of the simulation box for the networks composed of all polar atoms in $(NH_4)^+(Rha\text{-}C10C10)^-$ with water fractions of 0, 0.5 mol/mol of GL, 20 mol/mol of GL, and 100 mol/mol of GL are shown in Figure S16. The networks formed by polar atoms are obviously larger in both the amount and size, with the water fraction increasing from 0 to 0.5 mol/mol GL, also indicating that GL/water mixtures have a steadier structure inside. With much higher water fractions, HBs with anions have a much shorter lifetime that is only about half of a neat GL. Although 100 mol H_2O/mol of GL has the sharpest peak in Figure 9b and is enriched in polar networks, as shown in Figure S16, it is still dynamic according to the short HB lifetime. In one word, as the water fraction increases, the overall structure is more confined, but the subtle movements will increase.

Both the dynamics of the conformations and the HB occupancies, with different water fractions, show that (i) the structures are more confined when a small fraction of water is

https://doi.org/10.1021/acs.jpcb.2c07264
J. Phys. Chem. B 2023, 127, 921−931

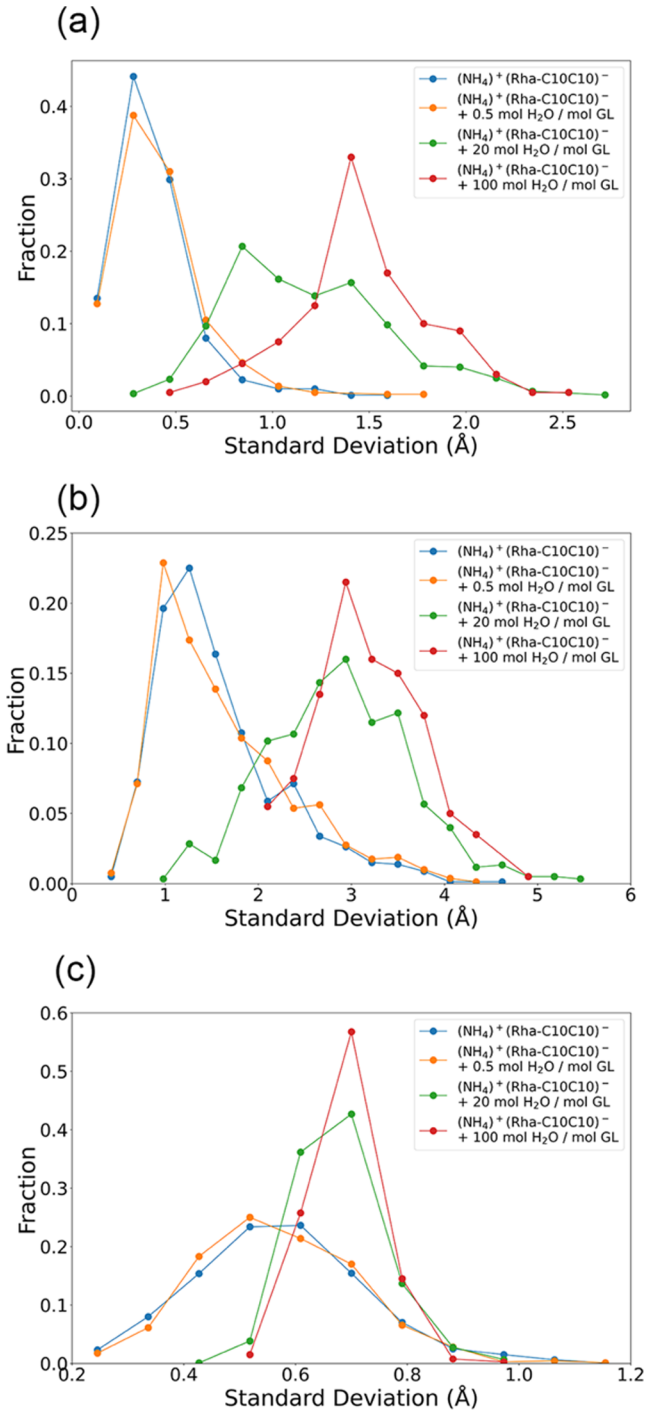

Figure 10. Standard deviation distributions of the nearest distance between carboxyl (O8, O9) and hydroxyl oxygens (O2, O3, O4) (a), the distance between two tails of alkyl chains (C10 and C20) (b), and the length of alkyl chains as measured by C3−C10 and C13−C20, respectively (c). The *Y*-axis is the fraction of molecules with that standard deviation.

added, and this explains the sharp increase; and (ii) the more dynamic structures and interactions when more water is added are actually not important to the conductivity. This is reasonable because −OH networks in GLs with 0 or 0.5 mol of water are small chunks and therefore sensitive to the dynamics, while the coverage ratio of −OH networks already reaches 1 at 20 and 100 mol of water fractions and the breaks and formations of branches do not dramatically affect the overall pathways.

4. CONCLUSIONS

In this work, we studied the impact of different water fractions and chemical compositions on conformations, dynamics, networks, and conductivities of ionic liquids formed from glycolipids. We find:

- The coverage ratio of the −OH networks inside the GLs provided a convenient qualitative way to determine the conductivity of a GL system, and the trend, where the first hydration layer is a turning point, matches the experimental results in the patent.
- Small addition of water enriched −OH networks by introducing significant hydrogen bonding to the system. It leads to a more confined structure. A higher FFV of the neat GLs provides space and interaction spots. These explain the sharp increase of conductivity with a small water fraction, as shown in the patent.
- We also investigated the effects of GL cations and anions on free volumes, vacancy distributions, and their relations to HB occupations. The tBuNH$_3^+$ can form more dedicated HBs, repelling other anions and leading to a larger FFV, and this contributes to a higher conductivity when water is added.
- The self-assembled structures are found in GLs, and with water fractions increasing, although the cations and anions are diluted, the −OH networks still grow larger. Limited solubility of tBuNH$_3^+$ helps it to decrease its migration and enriches the network structure. Meanwhile, the effects of dynamics and HB occupancies vary on different water fractions. With a small water fraction, GLs require stabilization for better conductivity, while after reaching the first hydration layer, it does not really matter, and this further explains the shape of the conductivity—water fraction curve.

■ ASSOCIATED CONTENT

Supporting Information

The Supporting Information is available free of charge at https://pubs.acs.org/doi/10.1021/acs.jpcb.2c07264.

Simulation result for the first hydration layer; simulation boxes for $(NH_4)^+$(Rha-C10)$^-$ and $(t$BuNH$_3)^+$(Rha-C10)$^-$; percolation and probe radius selection; snapshots of neat GL simulation boxes; snapshots of simulation boxes without −OH and boxes that only contain −OH from the same perspective for GLs with 20 and 100 mol water/mol of GL; the distributions of −OH networks at the x and y axes; snapshot of tBuNH$_3^+$ surrounded by four alkyl chains; the N−O RDF of $(NH_4)^+$(Rha-C10)$^-$, $(t$BuNH$_3)^+$(Rha-C10)$^-$, and $(NH_4)^+$(Rha-C10C10)$^-$; the C−C distributions of $(NH_4)^+$(Rha-C10)$^-$, $(NH_4)^+$(Rha-C10C10)$^-$, $(t$BuNH$_3)^+$(Rha-C10)$^-$, and $(t$BuNH$_3)^+$(Rha-C10C10)$^-$; six distances that are calculated to find the minimum distance between the carboxyl oxygens and hydroxyl oxygens; the HB occupancies of neat GLs; the N−O RDF of GLs with different fractions of excess neutral species; the HB occupancy of GLs with different excess neutral species; the HB occupancy of GLs with different fractions of water; and distributions of

https://doi.org/10.1021/acs.jpcb.2c07264
J. Phys. Chem. B 2023, 127, 921−931

networks composed of polar atoms in GLs with different fractions of water (PDF)

AUTHOR INFORMATION

Corresponding Author

Steven D. Schwartz − *Department of Chemistry and Biochemistry, University of Arizona, Tucson, Arizona 85721, United States;* orcid.org/0000-0002-0308-1059; Phone: 520 621 6363; Email: sschwartz@email.arizona.edu

Authors

Bai Hei − *Department of Chemistry and Biochemistry, University of Arizona, Tucson, Arizona 85721, United States*

Jeanne E. Pemberton − *Department of Chemistry and Biochemistry, University of Arizona, Tucson, Arizona 85721, United States;* orcid.org/0000-0002-1710-2922

Complete contact information is available at: https://pubs.acs.org/10.1021/acs.jpcb.2c07264

Author Contributions

The manuscript was written through contributions of all authors. All authors have given approval to the final version of the manuscript.

Notes

The authors declare no competing financial interest.

ACKNOWLEDGMENTS

All computations were performed on the University of Arizona High Performance Computing (HPC) facility. The authors gratefully acknowledge the support of this research through a grant award from the National Science Foundation (CHE-1954467).

ABBREVIATIONS

*t*BuNH$_2$, *tert*-butyl-amine; mRL, monorhamnolipid; Rha-C10, α-rhamnopyranosyl-β-hydroxydecanoate; Rha-C10C10, α-rhamnopyranosyl-β-hydroxydecanoyl-β-hydroxydecanoate

REFERENCES

(1) Somers, A. E.; Howlett, P. C.; MacFarlane, D. R.; Forsyth, M. A review of ionic liquid lubricants. *Lubricants* **2013**, *1*, 3−21.

(2) Lei, Z.; Chen, B.; Koo, Y.-M.; MacFarlane, D. R. Introduction: ionic liquids. *Chem. Rev.* **2017**, *117*, 6633−6635.

(3) Zhang, S.; Sun, N.; He, X.; Lu, X.; Zhang, X. Physical properties of ionic liquids: database and evaluation. *J. Phys. Chem. Ref. Data* **2006**, *35*, 1475−1517.

(4) Greaves, T. L.; Drummond, C. J. Protic ionic liquids: properties and applications. *Chem. Rev.* **2008**, *108*, 206−237.

(5) Chiappe, C.; Pieraccini, D. Ionic liquids: solvent properties and organic reactivity. *J. Phys. Org. Chem.* **2005**, *18*, 275−297.

(6) Yoshizawa, M.; Xu, W.; Angell, C. A. Ionic liquids by proton transfer: Vapor pressure, conductivity, and the relevance of Δp K a from aqueous solutions. *J. Am. Chem. Soc.* **2003**, *125*, 15411−15419.

(7) Belieres, J.-P.; Angell, C. A. Protic ionic liquids: preparation, characterization, and proton free energy level representation. *J. Phys. Chem. B* **2007**, *111*, 4926−4937.

(8) Mulligan, C. N. Environmental applications for biosurfactants. *Environ. Pollut.* **2005**, *133*, 183−198.

(9) Varjani, S. J.; Upasani, V. N. Critical review on biosurfactant analysis, purification and characterization using rhamnolipid as a model biosurfactant. *Bioresour. Technol.* **2017**, *232*, 389−397.

(10) Varjani, S. J.; Upasani, V. N. Core flood study for enhanced oil recovery through ex-situ bioaugmentation with thermo-and halotolerant rhamnolipid produced by Pseudomonas aeruginosa NCIM 5514. *Bioresour. Technol.* **2016**, *220*, 175−182.

(11) Hogan, D. E.; Curry, J. E.; Pemberton, J. E.; Maier, R. M. Rhamnolipid biosurfactant complexation of rare earth elements. *J. Hazard. Mater.* **2017**, *340*, 171−178.

(12) Yan, P.; Lu, M.; Yang, Q.; Zhang, H.-L.; Zhang, Z.-Z.; Chen, R. Oil recovery from refinery oily sludge using a rhamnolipid biosurfactant-producing Pseudomonas. *Bioresour. Technol.* **2012**, *116*, 24−28.

(13) Lee, M.-T. Micellization of Rhamnolipid Biosurfactants and Their Applications in Oil Recovery: Insights from Mesoscale Simulations. *J. Phys. Chem. B* **2021**, *125*, 9895−9909.

(14) Euston, S. R.; Banat, I. M.; Salek, K. Congener-dependent conformations of isolated rhamnolipids at the vacuum-water interface: A molecular dynamics simulation. *J. Colloid Interface Sci.* **2021**, *585*, 148−157.

(15) Munusamy, E.; Luft, C. M.; Pemberton, J. E.; Schwartz, S. D. Unraveling the differential aggregation of anionic and nonionic monorhamnolipids at air−water and oil−water Interfaces: a classical molecular dynamics simulation study. *J. Phys. Chem. B* **2018**, *122*, 6403−6416.

(16) Lu, G.; Zhang, X.; Shao, C.; Yang, H. Molecular dynamics simulation of adsorption of an oil-water-surfactant mixture on calcite surface. *Pet. Sci.* **2009**, *6*, 76−81.

(17) Eismin, R. J.; Munusamy, E.; Kegel, L. L.; Hogan, D. E.; Maier, R. M.; Schwartz, S. D.; Pemberton, J. E. Evolution of aggregate structure in solutions of anionic monorhamnolipids: Experimental and computational results. *Langmuir* **2017**, *33*, 7412−7424.

(18) Munusamy, E.; Luft, C. M.; Pemberton, J. E.; Schwartz, S. D. Structural properties of nonionic monorhamnolipid aggregates in water studied by classical molecular dynamics simulations. *J. Phys. Chem. B* **2017**, *121*, 5781−5793.

(19) Xuefen, Z.; Guiwu, L.; Xiaoming, W.; Hong, Y. Molecular dynamics investigation into the adsorption of oil−water−surfactant mixture on quartz. *Appl. Surf. Sci.* **2009**, *255*, 6493−6498.

(20) Chen, I.-C.; Lee, M.-T. Rhamnolipid Biosurfactants for Oil Recovery: Salt Effects on the Structural Properties Investigated by Mesoscale Simulations. *ACS Omega* **2022**, *7*, 6223−6237.

(21) Chen, M. L.; Penfold, J.; Thomas, R.; Smyth, T. J. P.; Perfumo, A.; Marchant, R.; Banat, I. M.; Stevenson, P.; Parry, A.; Tucker, I.; Grillo, I. Solution self-assembly and adsorption at the air−water interface of the monorhamnose and dirhamnose rhamnolipids and their mixtures. *Langmuir* **2010**, *26*, 18281−18292.

(22) Xie, Y.; Ye, R.; Liu, H. Microstructure studies on biosurfactant-rhamnolipid/n-butanol/water/n-heptane microemulsion system. *Colloids Surf., A* **2007**, *292*, 189−195.

(23) Pemberton, J. E.; Deodhar, B. S. Glyonic Liquids and Applications Thereof. U.S. Patent US202064202A1, 2022.

(24) Hayes, R.; Warr, G. G.; Atkin, R. Structure and nanostructure in ionic liquids. *Chem. Rev.* **2015**, *115*, 6357−6426.

(25) Mabuchi, T.; Tokumasu, T. Relationship between proton transport and morphology of perfluorosulfonic acid membranes: A reactive molecular dynamics approach. *J. Phys. Chem. B* **2018**, *122*, 5922−5932.

(26) Yoshida, T.; Tokumasu, T. Molecular dynamics study of proton transfer including Grotthus mechanism in polymer electrolyte membrane. *ECS Trans.* **2010**, *33*, No. 1055.

(27) Bernardes, C. E. S.; Minas da Piedade, M. E.; Canongia Lopes, J. N. The structure of aqueous solutions of a hydrophilic ionic liquid: The full concentration range of 1-ethyl-3-methylimidazolium ethylsulfate and water. *J. Phys. Chem. B* **2011**, *115*, 2067−2074.

(28) Liu, X.; O'Harra, K. E.; Bara, J. E.; Turner, C. H. Molecular insight into the anion effect and free volume effect of CO 2 solubility in multivalent ionic liquids. *Phys. Chem. Chem. Phys.* **2020**, *22*, 20618−20633.

(29) Ghoshdastidar, D.; Senapati, S. Ion-water wires in imidazolium-based ionic liquid/water solutions induce unique trends in density. *Soft Matter* **2016**, *12*, 3032−3045.

(30) Singh, A. P.; Gardas, R. L.; Senapati, S. Divergent trend in density versus viscosity of ionic liquid/water mixtures: a molecular view from guanidinium ionic liquids. *Phys. Chem. Chem. Phys.* **2015**, *17*, 25037−25048.
(31) Bailey, H. E.; Wang, Y.-L.; Fayer, M. D. Impact of hydrogen bonding on the dynamics and structure of protic ionic liquid/water binary mixtures. *J. Phys. Chem. B* **2017**, *121*, 8564−8576.
(32) Huang, Y.; Wan, Z.; Yang, Z.; Ji, Y.; Li, L.; Yang, D.; Zhu, M.; Chen, X. Concentration-dependent hydrogen bond behavior of ethylammonium nitrate protic ionic liquid−water mixtures explored by molecular dynamics simulations. *J. Chem. Eng. Data* **2017**, *62*, 2340−2349.
(33) Verma, A.; Stoppelman, J. P.; McDaniel, J. G. Tuning water networks via ionic liquid/water mixtures. *Int. J. Mol. Sci.* **2020**, *21*, 403.
(34) Serva, A.; Migliorati, V.; Lapi, A.; Aquilanti, G.; Arcovito, A.; D'Angelo, P. Structural properties of geminal dicationic ionic liquid/water mixtures: a theoretical and experimental insight. *Phys. Chem. Chem. Phys.* **2016**, *18*, 16544−16554.
(35) Bhargava, B. L.; Yasaka, Y.; Klein, M. L. Computational studies of room temperature ionic liquid−water mixtures. *Chem. Commun.* **2011**, *47*, 6228−6241.
(36) Migliorati, V.; Zitolo, A.; D'Angelo, P. Using a combined theoretical and experimental approach to understand the structure and dynamics of imidazolium-based ionic liquids/water mixtures. 1. MD simulations. *J. Phys. Chem. B* **2013**, *117*, 12505−12515.
(37) Hanke, C. G.; Lynden-Bell, R. A simulation study of water−dialkylimidazolium ionic liquid mixtures. *J. Phys. Chem. B* **2003**, *107*, 10873−10878.
(38) Feng, S.; Voth, G. A. Molecular dynamics simulations of imidazolium-based ionic liquid/water mixtures: Alkyl side chain length and anion effects. *Fluid Phase Equilib.* **2010**, *294*, 148−156.
(39) Niazi, A. A.; Rabideau, B. D.; Ismail, A. E. Effects of water concentration on the structural and diffusion properties of imidazolium-based ionic liquid−water mixtures. *J. Phys. Chem. B* **2013**, *117*, 1378−1388.
(40) Wang, Y.; Jiang, W.; Yan, T.; Voth, G. A. Understanding ionic liquids through atomistic and coarse-grained molecular dynamics simulations. *Acc. Chem. Res.* **2007**, *40*, 1193−1199.
(41) Komarov, P. V.; Khalatur, P. G.; Khokhlov, A. R. Large-scale atomistic and quantum-mechanical simulations of a Nafion membrane: Morphology, proton solvation and charge transport. *Beilstein J. Nanotechnol.* **2013**, *4*, 567−587.
(42) Okuwaki, K.; Mochizuki, Y.; Doi, H.; Kawada, S.; Ozawa, T.; Yasuoka, K. Theoretical analyses on water cluster structures in polymer electrolyte membrane by using dissipative particle dynamics simulations with fragment molecular orbital based effective parameters. *RSC Adv.* **2018**, *8*, 34582−34595.
(43) Canongia Lopes, J. N. A.; Pádua, A. A. Nanostructural organization in ionic liquids. *J. Phys. Chem. B* **2006**, *110*, 3330−3335.
(44) Marx, D. Proton transfer 200 years after von Grotthuss: Insights from ab initio simulations. *ChemPhysChem* **2006**, *7*, 1848−1870.
(45) Ingenmey, J.; Gehrke, S.; Kirchner, B. How to harvest Grotthuss diffusion in protic ionic liquid electrolyte systems. *ChemSusChem* **2018**, *11*, 1900−1910.
(46) Martínez, L.; Andrade, R.; Birgin, E. G.; Martínez, J. M. PACKMOL: a package for building initial configurations for molecular dynamics simulations. *J. Comput. Chem.* **2009**, *30*, 2157−2164.
(47) Phillips, J. C.; Hardy, D. J.; Maia, J. D.; Stone, J. E.; Ribeiro, J. V.; Bernardi, R. C.; Buch, R.; Fiorin, G.; Hénin, J.; Jiang, W.; et al. Scalable molecular dynamics on CPU and GPU architectures with NAMD. *J. Chem. Phys.* **2020**, *153*, No. 044130.
(48) Vanommeslaeghe, K.; Hatcher, E.; Acharya, C.; Kundu, S.; Zhong, S.; Shim, J.; Darian, E.; Guvench, O.; Lopes, P.; Vorobyov, I. CHARMM general force field: A force field for drug-like molecules compatible with the CHARMM all-atom additive biological force fields. *J. Comput. Chem.* **2010**, *31*, 671−690.
(49) Vanommeslaeghe, K.; MacKerell, A. D., Jr Automation of the CHARMM General Force Field (CGenFF) I: bond perception and atom typing. *J. Chem. Inf. Model.* **2012**, *52*, 3144−3154.
(50) Vanommeslaeghe, K.; Raman, E. P.; MacKerell, A. D., Jr Automation of the CHARMM General Force Field (CGenFF) II: assignment of bonded parameters and partial atomic charges. *J. Chem. Inf. Model.* **2012**, *52*, 3155−3168.
(51) Mayne, C. G.; Saam, J.; Schulten, K.; Tajkhorshid, E.; Gumbart, J. C. Rapid parameterization of small molecules using the force field toolkit. *J. Comput. Chem.* **2013**, *34*, 2757−2770.
(52) Luft, C. M.; Munusamy, E.; Pemberton, J. E.; Schwartz, S. D. A classical molecular dynamics simulation study of interfacial and bulk solution aggregation properties of dirhamnolipids. *J. Phys. Chem. B* **2020**, *124*, 814−827.
(53) Hanke, C. G.; Lynden-Bell, R. A simulation study of water−dialkylimidazolium ionic liquid mixtures. *J. Phys. Chem. B* **2003**, *107*, 10873−10878.
(54) Jiang, W.; Wang, Y.; Voth, G. A. Molecular dynamics simulation of nanostructural organization in ionic liquid/water mixtures. *J. Phys. Chem. B* **2007**, *111*, 4812−4818.
(55) Del Pópolo, M. G.; Mullan, C.; Holbrey, J.; Hardacre, C.; Ballone, P. Ion association in [bmim][PF6]/naphthalene mixtures: An experimental and computational study. *J. Am. Chem. Soc.* **2008**, *130*, 7032−7041.
(56) Liu, X.; Bara, J. E.; Turner, C. H. Understanding Gas Solubility of Pure Component and Binary Mixtures within Multivalent Ionic Liquids from Molecular Simulations. *J. Phys. Chem. B* **2021**, *125*, 8165−8174.
(57) Qiao, B.; Zhao, X.; Yue, D.; Zhang, L.; Wu, S. A combined experiment and molecular dynamics simulation study of hydrogen bonds and free volume in nitrile-butadiene rubber/hindered phenol damping mixtures. *J. Mater. Chem.* **2012**, *22*, 12339−12348.
(58) Beichel, W.; Yu, Y.; Dlubek, G.; Krause-Rehberg, R.; Pionteck, J.; Pfefferkorn, D.; Bulut, S.; Bejan, D.; Friedrich, C.; Krossing, I. Free volume in ionic liquids: a connection of experimentally accessible observables from PALS and PVT experiments with the molecular structure from XRD data. *Phys. Chem. Chem. Phys.* **2013**, *15*, 8821−8830.
(59) Van Swygenhoven, H.; Derlet, P. *Atomistic Simulations of Dislocations in FCC Metallic Nanocrystalline Materials*; Elsevier: Amsterdam, 2008.
(60) Bondi, Av. van der Waals volumes and radii. *J. Phys. Chem. A* **1964**, *68*, 441−451.
(61) Račko, D.; Capponi, S.; Alvarez, F.; Colmenero, J.; Bartoš, J. The free-volume structure of a polymer melt, poly (vinyl methylether) from molecular dynamics simulations and cavity analysis. *J. Chem. Phys.* **2009**, *131*, No. 064903.
(62) Pomès, R.; Roux, B. Molecular mechanism of H+ conduction in the single-file water chain of the gramicidin channel. *Biophys. J.* **2002**, *82*, 2304−2316.
(63) Zhang, Y.; Haider, K.; Kaur, D.; Ngo, V. A.; Cai, X.; Mao, J.; Khaniya, U.; Zhu, X.; Noskov, S.; Lazaridis, T.; Gunner, M. R. Characterizing the water wire in the Gramicidin channel found by Monte Carlo sampling using continuum electrostatics and in molecular dynamics trajectories with conventional or polarizable force fields. *J. Comput. Biophys. Chem.* **2021**, *20*, 111−130.
(64) Ichikawa, T.; Yoshio, M.; Hamasaki, A.; Mukai, T.; Ohno, H.; Kato, T. Self-organization of room-temperature ionic liquids exhibiting liquid-crystalline bicontinuous cubic phases: Formation of nano-ion channel networks. *J. Am. Chem. Soc.* **2007**, *129*, 10662−10663.

https://doi.org/10.1021/acs.jpcb.2c07264
J. Phys. Chem. B 2023, 127, 921−931